# A Method for Measuring Mode I Crack Tip Constraint Under Static and Dynamic Loading Conditions

by M.J. Maleski, M.S. Kirugulige and H.V. Tippur

ABSTRACT—A novel experimental technique for measuring crack tip *T*-stress, and hence in-plane crack tip constraint, in elastic materials has been developed. The method exploits optimal positioning of stacked strain gage rosette near a mode I crack tip such that the influence of dominant singular strains is negated in order to determine *T*-stress accurately. The method is demonstrated for quasi-static and low-velocity impact loading conditions and two values of crack length to plate width ratios (*a/W*). By coupling this new method with the Dally–Sanford single strain gage method for measuring the mode I stress intensity factor $K_I$, the crack tip biaxiality parameter $\beta = T\sqrt{\pi a}/K$ is also measured experimentally. Complementary small strain, static and dynamic finite element simulations are carried out under plane stress conditions. Time histories of $K_I$ and *T*-stress are computed by regression analysis of the displacement and stress fields, respectively. The experimental results are in good agreement with those obtained from numerical simulations. Preliminary data for critical values of $K_I$ and $\beta$ for dynamic experiments involving epoxy specimens are reported. Dynamic crack initiation toughness shows an increasing trend as $\beta$ becomes more negative at higher impact velocities.

KEY WORDS—Dynamic fracture, constraint, biaxilality, *T*-stress, strain gages, finite elements

## Introduction

In linear elastic fracture mechanics, the primary focus is generally on the stress intensity factor (SIF) as an engineering parameter that quantifies amplification of stresses ahead of the crack tip and the one that governs fracture response. However, several investigations[1,2] point to the potential significance of the non-singular constant stress term, $\sigma_{ox}$, as first coined by Irwin,[3] or the so-called *T*-stress term playing an important role in fracture processes such as crack growth stability, crack kinking, and critical SIF. Similar realization about the inadequacy of the *J*-integral alone as the elasto-plastic fracture parameter predates its elastic counterparts where the effect of the so-called non-singular *Q*-stress term has been recognized. Under small-scale yielding conditions, the use of *T*-stress in place of *Q*-stress has been recommended as well.[4] Until recently, this discussion was limited to quasi-static loading conditions and of late, the role of nonsingular stresses on fracture behavior under dynamic loading conditions has come under scrutiny as well.[5] Jayadevan et al.[6] have hypothesized that large negative *T*-stresses might be responsible for increasing dynamic crack initiation toughness at higher loading rates.

Earlier experimental attempts at utilizing $\sigma_{ox}$ for mode I cracks were in the context of evaluating $K_I$ accurately from photoelastic fringes by accounting for normal stress acting parallel to the crack. Difficulties with Irwin's method of coupling the $\partial\tau_{max}/\partial\theta|_{\theta=\theta_{max}} = 0$ condition when analyzing isochromatics representing in-plane maximum shear stress ($\tau_{max}$) contours gave way to several distinct methods. These methods have been reviewed in detail by Sanford.[7] Among these, overdeterministic least-squares analysis of measured full-field data using asymptotic crack tip field description[8,9] has become an accepted approach for evaluating $K_I$ accurately. Using such an approach, Chona et al.[8] were able to demonstrate that the singularity-dominated zone is dependent on specimen size. They have shown that the *K*-dominant zone is affected significantly by non-singular terms for deeply cracked specimens. The role of *T*-stress in crack curving and dynamic branching has also been noted by Ramulu and Kobayashi.[10] More recently, Sumter[11] has shown that two different geometries having the same *T*-stress will fail at the same value of the *J*-integral.

Among the analytical and numerical works, Larsson and Carlsson[12] have observed that the boundary layer solution of the elastic–plastic crack problem is not a meaningful representation of the real crack problem unless it is corrected for non-singular stress acting in the direction of the crack. Subsequently, Rice[13] has shown that the effect of *T*-stress is quite pronounced on the plastic zone size at the load levels corresponding to the American Society for Testing and Materials (ASTM) limit although the *T*-stress effect on near tip parameters such as the *J*-integral and crack tip opening displacements. Several numerical investigators subsequently have evaluated the non-singular *T*-stress by various methods. Kfouri[14] has shown that *T*-stress can be evaluated from finite element solutions by superimposing a known auxiliary field to the elastic *K*-field and augmenting it with the *J*-integral. The interaction integral method has been used by Nakamura and Parks[15] to evaluate *T*-stress along a three-dimensional (3D) crack front. Sladek et al.[16] have evaluated elasto-dynamic *T*-stress by using the interaction integral from the boundary element solution. A reasonably accurate estimation of *T*-stress by a relatively simple normal stress difference method has been demonstrated by Yang and Ravi-Chandar.[17]

*M.J. Maleski and M.S. Kirugulige (SEM members) are Graduate Students, and H.V. Tippur (SEM member; htippur@eng.auburn.edu) is an Alumni Professor, Department of Mechanical Engineering, 202 Ross Hall, Auburn University, AL 36830, USA.*

*Original manuscript submitted: January 12, 2004.*
*Final manuscript received: July 7, 2004.*
DOI: 10.1177/0014485104047610

In spite of these motivating factors, experimental techniques that are primarily aimed towards direct and accurate measurement of $T$-stress under static and dynamic loading conditions have been absent in the literature. As noted earlier, previous experimental works have generally focused on evaluating mode I SIFs accurately for studying the issue of $K$-dominance using single parameter fracture mechanics. In the current study, a strain gage measurement technique is proposed for evaluating the $T$-stress histories under static and impact loading conditions directly from the experiments. By coupling this new method with the Dally–Sanford single strain gage method[18,19] for $K_I$ determination, in-plane constraint or biaxiality parameter histories have been determined under mode I conditions. Complementary finite element simulations are used to validate the approach independently. Some of the preliminary dynamic crack initiation data along with measured constraint values are also reported.

## Proposed Method: Theoretical Basis

The asymptotic description for crack tip normal and shear strains near a mode I crack in a planar elastic body is given by[20,21]

$$E\epsilon_{xx} = A_1 r^{-1/2}\cos\frac{\theta}{2}\left[(1-\nu)-(1+\nu)\sin\frac{\theta}{2}\sin\frac{3\theta}{2}\right] + 2A_2 r^0 + A_3 r^{1/2}\cos\frac{\theta}{2}\left[(1-\nu)+(1+\nu)\sin^2\frac{\theta}{2}\right] + 2A_4 r^1\cos\theta + ..., \quad (1)$$

$$E\epsilon_{yy} = A_1 r^{-1/2}\cos\frac{\theta}{2}\left[(1-\nu)+(1+\nu)\sin\frac{\theta}{2}\sin\frac{3\theta}{2}\right] - 2\nu A_2 r^0 + A_3 r^{1/2}\cos\frac{\theta}{2}\left[(1-\nu)-(1+\nu)\sin^2\frac{\theta}{2}\right] - 2\nu A_4 r^1\cos\theta + ..., \quad (2)$$

$$E\gamma_{xy} = A_1(1+\nu)r^{-1/2}\sin\theta\cos\frac{3\theta}{2} - A_2(1+\nu)r^{1/2}\sin\theta\cos\frac{\theta}{2} - 2A_4(1+\nu)r\sin\theta, \quad (3)$$

where $(x, y)$ and $(r, \theta)$ are the crack tip Cartesian and polar coordinates (see Fig. 1), and $E$ and $\nu$ denote the elastic modulus and the Poisson ratio, respectively. In eqs (1)–(3), the coefficient of the expansion $A_1$ is proportional to the mode I SIF, $K_I$, and $A_2$ to the $T$-stress. In the above equations for strain components, the series is truncated after the first four terms with an implication that it would provide sufficient accuracy for describing the near tip strain fields in finite size samples with edge cracks.

Using the above equations, normal strain difference $(\epsilon_{xx} - \epsilon_{yy})$ can be written as

$$E(\epsilon_{xx}-\epsilon_{yy}) = -2A_1 r^{-1/2}(1+\nu)\cos\frac{\theta}{2}\sin\frac{\theta}{2}\sin\frac{3\theta}{2} + 2A_2(1+\nu) + 2A_3 r^{1/2}(1+\nu)\cos\frac{\theta}{2}\sin^2\frac{\theta}{2} + 2(1+\nu)A_4 r^1\cos\theta. \quad (4)$$

By using coordinate transformation equations, the normal strain difference can be expressed in polar coordinates rotated by an angle $\alpha$ as

$$E(\epsilon_{rr}-\epsilon_{\theta\theta}) = A_1(1+\nu)r^{-1/2}\sin\theta\left[\cos\frac{3\theta}{2}\sin 2\alpha - \sin\frac{3\theta}{2}\cos 2\alpha\right] + 2A_2(1+\nu)\cos 2\alpha + A_3(1+\nu)r^{1/2}\sin\theta\left[\sin\frac{\theta}{2}\cos 2\alpha - \cos\frac{\theta}{2}\cos 2\alpha\right] + 2A_4(1+\nu)r^1[\cos\theta\cos 2\alpha - 2\sin\theta\sin 2\alpha]. \quad (5)$$

It is instructive to plot eqs (4) and (5) as a function of $\theta$ to examine variations of normal strain differences in Cartesian and polar coordinates. Such a variation is presented in Fig. 2 where the angle $\alpha$ is made to coincide with $\theta$, and the Poisson ratio of 1/3 is used. It can be seen from Fig. 2(a) that three values of $\theta$, ($\theta = 0, \pm 2\pi/3, \pm\pi$) yield expressions where the dominant coefficient $A_1$ in the series can be eliminated by considering the difference of the normal strains $(\epsilon_{xx} - \epsilon_{yy})$. If one were to use a two-term description of the crack tip strain field, the natural elimination of the dominant coefficient $A_1$ along these directions could be exploited for determining the second term of the expansion, namely the $T$-stress. It should be noted that the angle $\theta = \pm\pi$ is not a feasible choice due to the practical difficulty in affixing strain gages on the crack faces.

The other two choices for the angle $\theta$, namely 0 and $\pm 2\pi/3$, are indeed feasible if measurements are made outside the region of dominant 3D effects. It should be emphasized at this point that the strain difference values in finite-dimensional samples should be measured at distances beyond $r = 0.5B$, where $B$ is the plate thickness in order to avoid crack tip 3D effects. This imposes an additional degree of difficulty for performing measurements. Previous studies[9,22] have shown that the 3D effects extend ahead of the crack tip and in the region adjacent to the crack flanks as shown in Fig. 3.[†] The contour plots in Fig. 3 represent the plane strain constraint $\sigma_{zz}/(\nu(\sigma_{xx} + \sigma_{yy}))$ which assumes a value of $\pm 1$ for plane strain conditions and zero for plane stress conditions. Even though the terms in the series associated with $r^{-1/2}, r^{1/2}, r^{3/2}, ...$ all vanish for $\theta = 0°$, obtaining a reasonably accurate strain difference from the gages in this direction will be difficult due to 3D effects. It can be seen from Fig. 3 that the 3D region extends farther along $\theta = 0°$ compared to $\theta = 120°$. Also, the plane stress conditions prevail at relatively small distances in the sector $\pm 90° < \theta < \pm 135°$ around the crack tip with $\theta \approx 120°$ being the most optimum angle in order to avoid 3D effects. These observations are used frequently while analyzing crack tip fringes obtained using the method of Coherent Gradient Sensing (CGS).[23]

A similar investigation of strains in polar coordinates, as shown in Fig. 2(b), is also carried out. It is evident from this plot that the term associated with $r^{-1/2}$ remains dominant throughout except at $\theta = 0°$ and $\pm 180°$, which are not good choices for the reasons mentioned above. Hence, normal strain difference $(\epsilon_{rr} - \epsilon_{\theta\theta})$ based measurements are not pursued during this work.

[†]A 3D elasto-static finite element simulation was carried out to obtain this plot. The details are avoided here for brevity and similar results can be found elsewhere.[9]

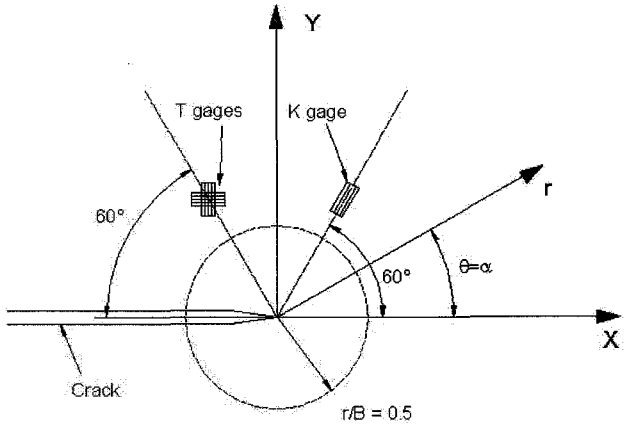


Fig. 1. Schematic diagram for locating the strain gages near a mode I crack for determining $T$-stress and $K_I$

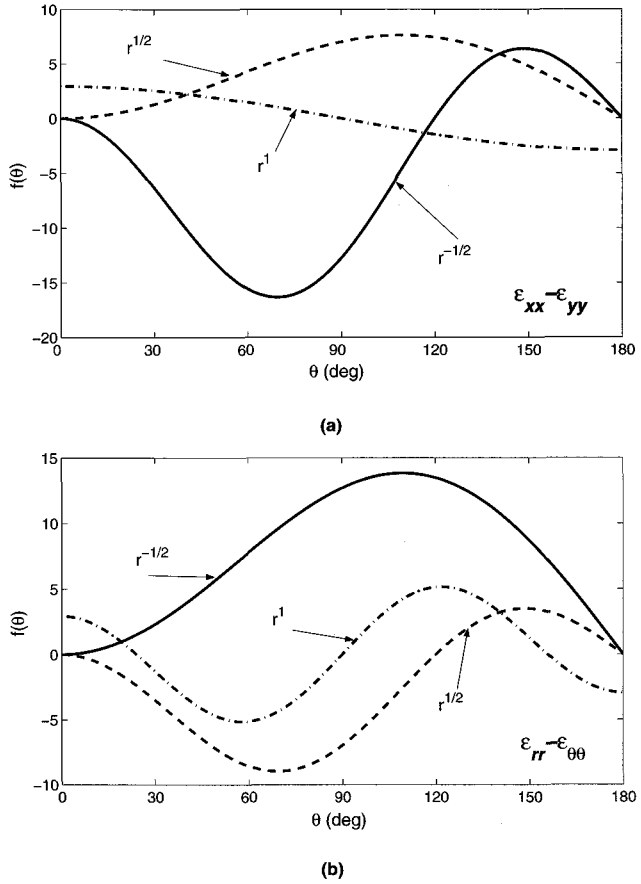


Fig. 2. Normal strain difference plots in (a) rectangular (eq (4)) and (b) polar coordinates (eq (5)) to investigate the feasibility of extracting $T$-stress by using strain gage rosettes

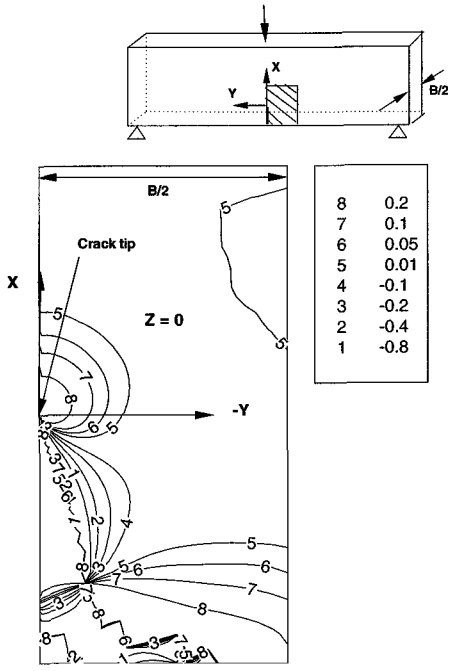


Fig. 3. Crack tip triaxiality in static TPB specimen in terms of the plane strain constraint parameter $\sigma_{zz}/(\nu(\sigma_{xx}+\sigma_{yy}))$ on the mid-plane

Substituting $\theta = 120°$ in eq (4) yields the following relation for normal strain difference in Cartesian coordinate system:

$$\frac{E}{1+\nu}(\epsilon_{xx}-\epsilon_{yy}) \approx 2A_2 + \frac{3A_3 r^{1/2}}{4} - A_4 r. \qquad (6)$$

Here, to evaluate $T$-stress proportional to $A_2$, we can make two levels of approximations: truncate the series beyond the $r^o$ term (two-term approximation) or beyond the $r^{1/2}$ term (three-term approximation) in eq (6). The former approximation leads to

$$\frac{E}{1+\nu}(\epsilon_{xx}-\epsilon_{yy}) \approx 2A_2, \qquad (7)$$

while the latter leads to

$$\frac{E}{1+\nu}(\epsilon_{xx}-\epsilon_{yy}) \approx 2A_2 + \frac{3A_3 r^{1/2}}{4}. \qquad (8)$$

The two-term approximation requires a strain difference measurement at a single point in the crack tip vicinity. The three-term approximation, on the other hand, needs strain difference measurements from at least two discrete locations near the crack tip. Further, the measured data of $(E/1+\nu)(\epsilon_{xx}-\epsilon_{yy})$ needs to be plotted as a function of $\sqrt{r}$ and fitted as a straight line, and extrapolated to the crack tip ($r=0$) in order to evaluate the crack tip $T$-stress.

## Measurement of $K_I$: Dally–Sanford Method

Using eq (1) and strain-transformation equations, the asymptotic description for radial strain $\epsilon_{rr}$ in the angular direction near the crack tip is

$$\frac{E}{(1+\nu)}\epsilon_{rr}(r,\theta) = C_1 r^{-1/2} g_1(\theta,\alpha,\nu) + C_2 r^0 g_2(\theta,\alpha,\nu) + C_3 r^{1/2} g_3(\theta,\alpha,\nu) + \ldots, \quad (9)$$

where the functions $g_1$–$g_3$ are given by

$$g_1 = \kappa\cos\frac{\theta}{2} - \frac{1}{2}\sin\theta\left(\sin\frac{3\theta}{2}\cos 2\alpha - \cos\frac{3\theta}{2}\sin 2\alpha\right) \quad (10)$$

$$g_2 = \kappa + \cos 2\alpha \quad (11)$$

$$g_3 = \cos\frac{\theta}{2}\left(\kappa + \sin^2\frac{\theta}{2}\cos 2\alpha - \frac{1}{2}\sin\theta\sin 2\alpha\right) \quad (12)$$

and

$$\kappa = \frac{1-\nu}{1+\nu}$$

for plane stress. Using the first three terms of the asymptotic expansion, it has been shown[18] that a single strain gage can be used to determine the mode I SIF accurately if the gage is positioned beyond the region of dominant triaxial effects. It is shown that, for materials with a Poisson ratio of 1/3, the angular orientation of such a gage simplifies to $\alpha = \pm\pi/3$ and is marginally different for other common engineering materials. A tabulation of $\alpha$ for different $\nu$ values can be found in Dally and Sanford.[18] Under these circumstances, the strain gage signals are directly proportional to the mode I SIF:

$$K_I = E\epsilon_{rr}\sqrt{(8/3)\pi r}. \quad (13)$$

## Static Experiments

### Sample Preparation

Edge-cracked epoxy samples with dimensions that satisfy beam characteristics were developed for experimentation. For each sample, an edge notch was created at the mid-span of the beam as shown in Fig. 4. The specimen material was a low-viscosity epoxy resin polymerized using an amine-based hardener. The resin–hardener mixture for each sample was prepared and poured into a mold such that all test specimens had the same span and thickness. The crack was introduced using a precisely sharpened blade placed within the mold prior to pouring the epoxy resin. Once the resin had cured, the blade could then be removed leaving a "sharp" crack at the mid-span of the beam. This method of producing a sharp crack was found to be very repeatable. A photograph of the crack tip thus formed is shown in Fig. 5. The beams were machined to the dimensions shown in Fig. 4.

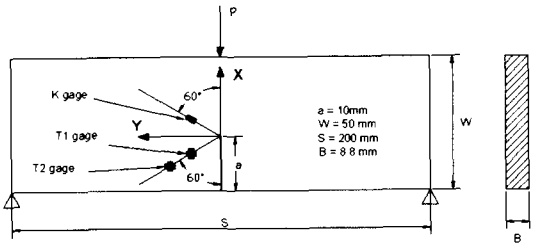


Fig. 4. Schematic diagram of the specimen geometry along with loading configurations for static experiments ($a/W = 0.2$)

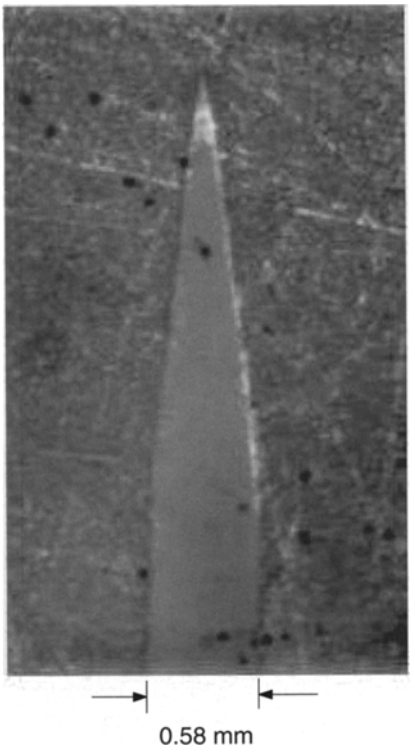


Fig. 5. Magnified view of the crack tip created using a sharpened blade

### Evaluation of $K_I$ and $T$

Stacked 0°–90° strain gage rosettes (henceforth referred to as $T$-gages) were mounted along $\theta = 120°$ in the $x$–$y$ directions as shown in Fig. 4. The individual strain gages of the 0°–90° rosette were connected to the arms of a standard Wheatstone bridge circuit in a half-bridge configuration. The choice

of half-bridge allows direct, temperature compensated, normal strain difference ($\epsilon_{xx} - \epsilon_{yy}$) measurement needed for $T$-stress determination using eq (7) or eq (8) with two-term or three-term approximation, respectively. A single strain gage (henceforth referred to as the $K$-gage) along $\theta = 60°$ was also fixed in the radial direction for measuring the mode I SIF. In order to minimize the strain averaging effects, the smallest commercially available gages (gage length 0.8 mm, gage factor 2.11) (CEA-13-032WT-120, Vishay-Micromeasurements Group, Inc.) were used.

For the static experiments, the beams with a crack length to specimen width ratio ($a/W$) of 0.2 were prepared. The beams were loaded in three-point bend (TPB) configuration. The strains from gages along 60° and 120° were recorded for each load increment. The experimental results were obtained using measured strain signals and eqs (7) and (8). The Young modulus and Poisson ratio used were 3.2 GPa and 0.35, respectively. The SIF was also independently calculated using following equation[24]

$$K_I = \frac{3P\frac{S}{W}\sqrt{\frac{a}{W}}}{2B\sqrt{W}\left(1+2\frac{a}{W}\right)\left(1-\frac{a}{W}\right)^{3/2}} \left[1.99 - \frac{a}{W}\left(1-\frac{a}{W}\right)\left(2.15 - 3.93\frac{a}{W} + 2.7\frac{a^2}{W^2}\right)\right], \quad (14)$$

where $P$ is the applied static load. The experimental results were then compared to the theoretical values predicted.

### Results

The mode I SIFs computed from the $K$-gage output using eq (13) are plotted along with the predicted ones from eq (14) in Fig. 6(a). The measurements show excellent linearity with respect to the applied load. The measured values are within 10% of the predictions.

Data collected from the stacked strain gage rosettes along $\theta = 120°$ yielded strains used for calculating $T$-stress in three different ways. First, the values of $T$-stress were calculated from two individual rosettes (mounted at radii of 5.5 mm ($r/B$=0.63) and 10.5 mm ($r/B$=1.2), respectively, along the 120° line from the crack tip) assuming only two terms of the asymptotic expansion (see eq (7)). Secondly, an extrapolated value of $T$-stress was determined assuming a series truncation after three terms according to eq (8). These three values were then compared with the predicted values of the $T$-stress, namely the results of a finite element simulation, for the most suitable method. The details of the finite element simulations are discussed in the Finite Element Simulations Section. It was seen that the two-term expansion with a single gage mounted close to the crack tip (5.5 mm) is most suitable for obtaining consistent and accurate values of $T$-stress. The $T$-gage located at the larger distance from the crack tip introduced greater amounts of error due to diminutive strain signals in the region as well as its closeness to the sample edge. The single $T$-gage values were used to calculate the in-plane constraint values for each respective static load. The corresponding crack tip $\beta$ was determined for each load as $\beta = T\sqrt{\pi a}/K_I$ and are plotted in Fig. 6(b). The magnitude of $\beta$ for the range of loads considered is essentially constant and matches, within 6% difference, the computed values for

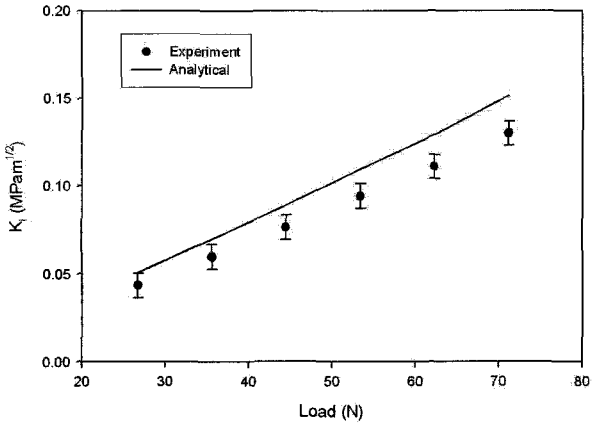


(a)

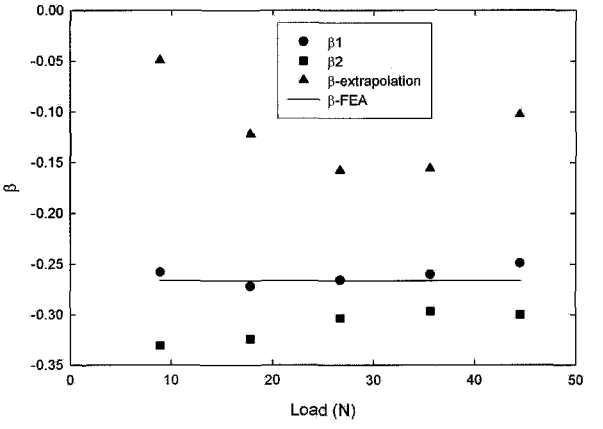


(b)

Fig. 6. Static experimental results compared with predicted values for $a/W$ = 0.2: (a) $K_I$ with load; (b) biaxiality parameter $\beta$ with load. $\beta_1$ and $\beta_2$ are from gages $T_1$ and $T_2$ (see Fig. 4)

the exact cracked geometry using finite elements. The $\beta_1$ values of −0.26 to −0.27 can be noted from Fig. 6(b). This is also in good agreement with the results reported by Kafouri[14] for the TPB specimen.

## Dynamic Experiments

### Experimental Details

Dynamic tests were performed on samples with $a/W = 0.2$ and $a/W = 0.5$. A Dynatup 9250-HV drop tower was used for impacting the specimens. This drop tower allowed for variable target velocities ranging from 0 to 20 m s$^{-1}$. The tower was also fitted with instrumented tup and anvils for recording impact force and support reactions. These forces were recorded throughout the event, triggered by an optically tripped flag, and used as input forcing functions for elastodynamic finite element simulations. During the experiment,

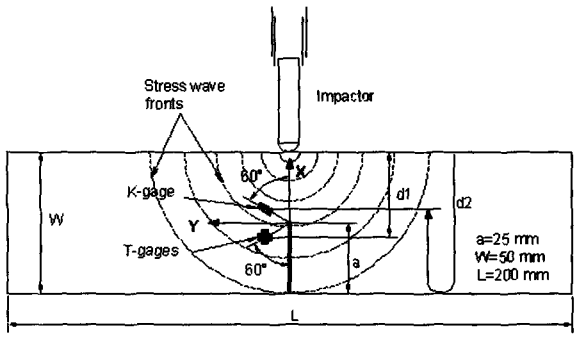


Fig. 7. Schematic diagram showing specimen geometry and loading configuration used in dynamic impact tests ($a/W$ = 0.5)

the sample was rested on a block of soft foam base such that the dynamic impact tests could be modeled as the single-point impact of a free–free beam. The specimen geometry and loading configuration (for $a/W = 0.5$) are shown in Fig. 7.

The impactor loads the specimen along the top edge of the beam directly above the crack. For the test configuration in the drop tower, the height of the impactor, $h$, is zero as the tip of the impactor makes the initial contact with the specimen. This reference point, $h = 0$, will allow the device to calculate the height needed to obtain the desired impact velocity. In this research, two velocities were chosen, $v = 1.5$ and 7 m s$^{-1}$, for two values of $a/W$ ratios, $a/W = 0.2$ and 0.5. (Higher crack velocities could not be employed due to the localized crushing of epoxy at the impact point.)

The $K_I$ and $T$-stress measurements were performed in the same manner as in the static tests. One gage mounted at $\theta = 60°$ on the specimen surface recorded the strain history for $K_I$ determination, and one 0°–90° stacked rosette mounted along $\theta = 120°$ recorded the strain history for $T$-stress calculations. The gage was located at $r = 5.5$ mm, as this was found optimal during static tests. The strain signals were converted into SIF $K_I$ and $T$-stress histories using eqs (13) and (7), respectively. In doing so, it is assumed that inertial effects enter the coefficients of the asymptotic expansion without altering the functional form of the equation.

The strain gage signal conditioner/amplifier model 563H, manufactured by Ectron, Inc., was selected for amplifying the stain gage signals. This device offers analog multichannel signal conditioning, and each channel has independent variable amplification and filtering. The amplification factor or gain can be set to increase the signal to 10–1000 times the actual output. The low-pass filter allows for noise reduction in the range of 10 Hz to 100 kHz. The unit has variable excitation option and the channels can be easily modified, to suit quarter-, half- or full-Wheatstone bridge configuration. The strain gage signals were acquired using an analog dynamic signal conditioning unit coupled to a PC-based multichannel digital data acquisition system from National Instruments, Inc. The data acquisition system used was capable of simultaneously acquiring signals at a rate of $5 \times 10^6$ samples s$^{-1}$ in up to four channels.

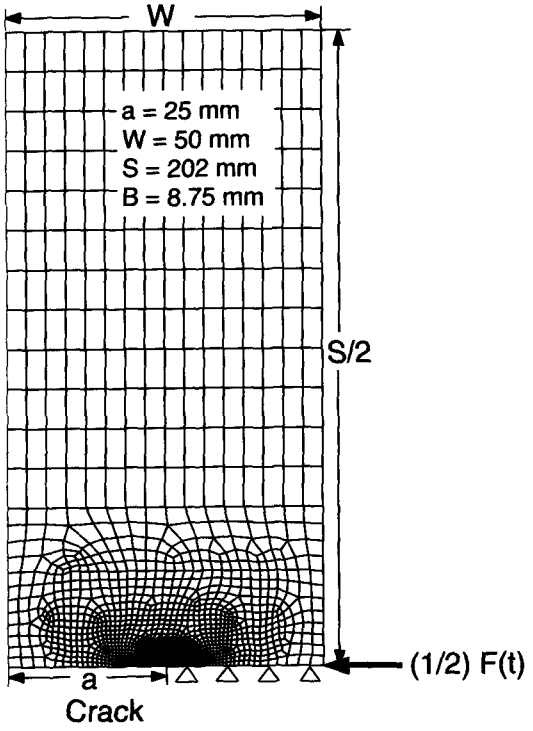


Fig. 8. Finite element mesh used for elasto-dynamic simulations ($a/W$ = 0.5)

### *Finite Element Simulations*

Finite element simulations were performed under plane stress conditions for static as well as for dynamic loading conditions. The static simulations were used to compute the in-plane biaxiality parameter β for the TPB specimens. The β values thus computed were compared with those in the literature, thereby optimizing the strain gage location for measuring $T$-stress. The method that agreed closely with the static simulation results was used for dynamic measurements.

Elasto-dynamic finite element simulations were aimed towards providing independent reference data for dynamic strain histories and verifying the proposed method for achieving transient values of $K_I$ and $T$-stress. The numerical model dimensions met the dimensions of one-half of the test specimen with the $a/W$ ratio of 0.2 or 0.5. A typical finite element mesh of the half model is shown in Fig. 8 along with loading and boundary conditions. The model dimensions were $102 \times 50$ mm$^2$ with a crack length of 25 mm for $a/W = 0.5$. The model consisted of 2350 isoparametric four-noded elements. The typical element size near the crack tip was less than 10% of the plastic zone radius at crack initiation or $(1/500)a$, where $a$ is initial crack length. Experimentally determined material properties of the Young modulus ($E = 4.37$ GPa), Poisson ratio ($\nu = 0.353$), and mass density ($\rho$=1139 kg m$^{-3}$) were used as input for finite element analysis.

The model was loaded using the force history recorded by the instrumented tup of the drop tower. One-half of the force was applied to the finite element simulation in view of the symmetric conditions. Also, the time-step of the force history measurement was larger than the time-step used in the

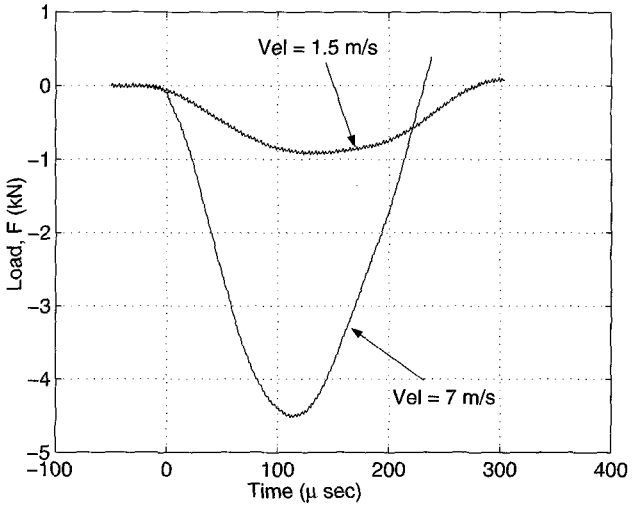


Fig. 9. Typical load histories recorded from Dynatup 9250-HV impactor

numerical study. Therefore, the recorded force history plot from the impactor was fitted with a polynomial function so that the force could be calculated for smaller time-steps. Considerable care was taken about the deviations while fitting the curve so that the force input indeed represents the actual force history given by the impactor. Representative force histories as given by the impactor for velocities 1.5 and 7 m $s^{-1}$ are shown in Fig. 9.

The time-step size in the finite element simulation was chosen considering the size of the smallest element contained in the discretized model. The time-step was calculated such that the stress wave propagation across any given element would not occur in less than three time-step iterations. Thus, the time-step size $\Delta t < (1/3)\Delta L/C_L$ was chosen where $\Delta L$ is the smallest element size in the mesh and $C_L$ is the longitudinal wave speed for the material. The implicit time integration scheme of the Newmark β method with Newmark parameters $\beta = 0.25$ and $\gamma = 0.5$ with 0.5% damping was adopted in the simulations. The simulation results were used for obtaining instantaneous SIFs $K_I$ and $T$-stress up to crack initiation.

The results of the finite element simulation were used to calculate the values of $K_I$ and $T$-stress over the time duration of force input. The transient values of the SIF were obtained using crack opening displacements. Examining the first two terms of the asymptotic expansion, using $K$-dominant approach close to the crack tip along $\theta = \pm\pi$, $K_I$ can be expressed in terms of $v$ displacement in the $y$-direction as

$$\left[(K_I)_{app}\right]_{\theta=\pm\pi} = K_I - Cr^{1/2} \tag{15}$$

where

$$(K_I)_{app} = \frac{Ev\sqrt{2\pi}}{4\sqrt{r}} \tag{16}$$

and $K_I$ is the SIF. The above represents a linear relationship between $(K_I)_{app}$ and $r$ with slope $C$ and the $y$-intercept $K_I$. By plotting $(K_I)_{app}$ as a function of $r$, we can obtain an

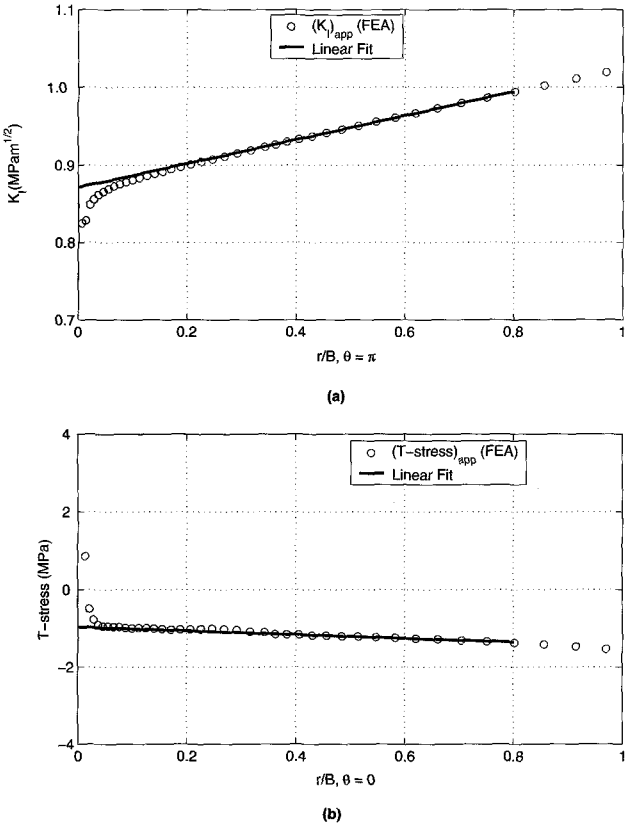


Fig. 10. Typical linear regression of finite element data to determine (a) $K_I$ using the crack flank displacement method, and (b) $T$-stress using the modified stress difference method

extrapolated value of $(K_I)_{app}$ at $r = 0$ as $K_I$. This is illustrated in Fig. 10(a). The linear portion of the curve has been extrapolated back to obtain $K_I$.

$T$-stress was determined from a modified stress difference method. The normal stress difference ahead of the crack is given by

$$\left[\sigma_{xx} - \sigma_{yy}\right]_{\theta=0} = T + Dr \tag{17}$$

where $D$ is the higher-order coefficient associated with the $r^1$ term in the asymptotic expansion for $(\sigma_{xx} - \sigma_{yy})$. The above represents a linear relationship between $(\sigma_{xx} - \sigma_{yy})$ and $(r)_{\theta=0^\circ}$ with slope $D$ and $T$-stress being the $y$-intercept of a linear fit of normal stress difference data. This is demonstrated in Fig. 10(b). It can be seen from Figs. 10(a) and (b) that $K_I$ and $T$ have very good linearity in the range where the straight line was fit. This process was repeated for all the time-steps to obtain the time history of $K_I$ and $T$-stress. The biaxiality parameter β was computed for each time-step using the relation $\beta = T\sqrt{\pi a}/K_I$.

## Results

Before discussing the results of dynamic impact tests and the corresponding finite element simulations, it is important to establish a common time base for the two independent analyses. The time base was determined to originate ($t = 0$) at impact as given by the velocity flag of the impactor. However, it should be noted here that the strain histories were

recorded separately and were not dependent on the velocity flag trigger. The strain recordings were based on a rising slope trigger ($0.2V$) of the $K$-gage initially set in the data acquisition software. The recording of strains from $T$-gages was based on triggering of the $K$-gage. A number of pre-trigger scans were specified so that the strain histories are recorded even before the strain signal of $K$-gage reaches $0.2V$.

The longitudinal stress wave speed for epoxy (approximately 2500 m s$^{-1}$) was used to calculate the time for stress waves to travel from the impact point to the different strain gage locations (see Fig. 7). Using this, the strain history plots were shifted with respect to the time base for correspondence with the tup force history. The tup force history serves as the time base for the complementary finite element simulations also.

The strain histories recorded by the $K$-gage and $T$-gages are shown in Figs. 11(a) and (b), respectively, for $a/W = 0.2$ and $V = 1.5$ m s$^{-1}$. It can be seen from this figure that the crack tip signal begins to rise with a time delay of approximately 25 μs after the impact for the $K_I$ gage and 17 μs for the $T$-gage based on the travel distances of $d_2$ and $d_1$, respectively, for $a/W = 0.2$. After this, the strain signal monotonically increases until about 200 μs (see Fig. 11(a)) followed by a sudden drop which indicates crack initiation. Good repeatability between two similar experiments can be seen from these plots. Similar strain history variations are presented for $a/W = 0.2$ and $V = 7.0$ m s$^{-1}$ in Figs. 12(a) and (b), respectively. The higher strain rates can be noted from this figure compared to $V = 1.5$ m s$^{-1}$. The crack initiation takes place at about 96 μ s indicating higher crack tip loading rate.

The time histories of $T$-stress and β corresponding to $a/W = 0.2$ are plotted in Fig. 13 for an impact velocity of 1.5 m s$^{-1}$. The corresponding finite element results are also shown in the same figure. It can be noted from Fig. 13(a) that the $T$-stress measured by the new method is in excellent agreement with that predicted by finite element simulations all the way up to the crack initiation point. Figure 13(b) shows the values of β computed by making use of the Dally–Sanford method in conjunction with the present method. The large negative β can be observed at initial stages. However, at later stages β levels off just before crack initiation. This trend can also be seen in the numerical simulations reported by Jayadevan et al.[6] Similar variations for impact velocity 7.0 m s$^{-1}$ are shown in Fig. 14. An increase in the biaxiality parameter β from −0.317 to −0.490 at crack initiation can be noted when impact velocity increases from 1.5 to 7.0 m s$^{-1}$.

The time histories of β for $a/W = 0.5$ are shown in Figs. 15(a) and (b) corresponding to impact velocities of 1.5 and 7.0 m s$^{-1}$, respectively. Compared with the results for $a/W = 0.2$, it can be seen that β is more negative for deeply cracked geometries. For deeply cracked specimens, the discrepancy between experiment and the predicted results is somewhat larger compared to shallow cracked geometries, as can be seen from Figs. 15(a) and (b). This can be attributed to the following factors. First, it should be noted here that $K$-dominance is strong in shallow cracked specimens compared to deeply cracked specimens. This can be seen in the full-field optical measurements of the crack tip fields reported by Tippur et al.[9] for an $a/W$ ratio of 0.2. Secondly, in the present study, the impact point interaction with the crack tip is more pronounced for deeply cracked specimens at times close to crack initiation.

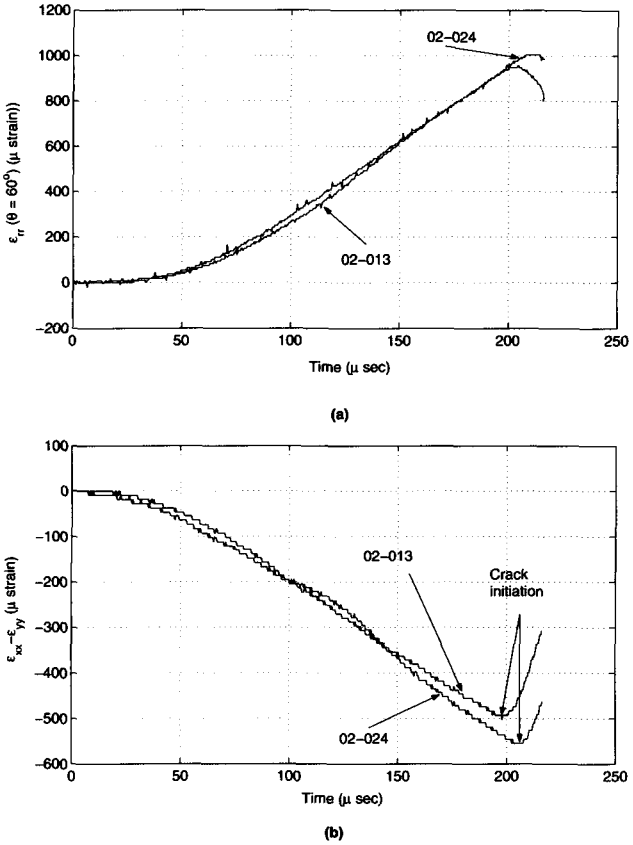


Fig. 11. Typical strain histories for (a) $K_I$ and (b) $T$-gages for two different specimens (02-013 and 02-024) with $a/W = 0.2$ and $V = 1.5$ m s$^{-1}$

The results from a few successful tests for each $a/W$ ratio and impact velocity are tabulated in Table 1. In all these experiments, the crack propagated in a self-similar fashion and no significant deviation in crack path was observed. The fracture parameters presented are crack tip loading rate $\dot{K}$ just before crack initiation, crack initiation toughness $K_{IC}$, $T$-stress and biaxiality parameter β at initiation. Before discussing these results, it should be noted that the static values of β are approximately −0.27 and +0.12, respectively, for $a/W$ 0.2 and 0.5 in TPB configurations as determined from static finite element simulations. The static value of $K_{IC}$ for the epoxy specimen used here is known to be in the range 0.9–1.0 MPa $\sqrt{\text{m}}$. Looking at the results of $a/W$=0.2 and $V = 1.5$ m s$^{-1}$, it can be seen that β values are slightly more negative compared with their static counterparts. Comparing these results with high-velocity tests, it can be observed that β becomes more negative with a marginal enhancement in $K_{IC}$. This is consistent with the prediction that mode I fracture toughness increases with negative $T$-stress for brittle materials.[25]

Comparing the results of $a/W$=0.2 and impact velocity 1.5 m s$^{-1}$ with $a/W$=0.5 and impact velocity of 7.0 m s$^{-1}$, it can be noted that $K_{IC}$ increases noticeably for the latter case. The reason for this could be twofold. First, the crack tip experiences a higher rate of loading in the deeply cracked configuration compared with shallow one for the same impact velocity. This can be seen from the table where the value of $\dot{K}$ for deeply cracked samples is more than $9 \times 10^3$ MPa $\sqrt{\text{m}}$ s$^{-1}$ compared to that for shallow cracked samples,

TABLE 1—SUMMARY OF $\dot{K}_I$, $K_I$, $T$, AND $\beta$ FROM DYNAMIC EXPERIMENTS

| | | | Parameters at Crack Initiation | | | |
|---|---|---|---|---|---|---|
| $a/W$ | Velocity of Impact | Sample Number | $\dot{K}_I$ (MPA $\sqrt{\text{m}}$ $\text{s}^{-1}$) | $K_I$ (MPa $\sqrt{\text{m}}$) | $T$ (MPa) | $\beta = (T\sqrt{\pi a}/K_I)$ |
| 0.2 | 1.5 m $\text{s}^{-1}$ | 02-012 | $6.09 \times 10^3$ | 0.99 | −1.84 | −0.317 |
| | | 02-013 | $6.23 \times 10^3$ | 0.98 | −1.77 | −0.313 |
| | | 02-024 | $6.26 \times 10^3$ | 0.94 | −1.81 | −0.328 |
| | 7.0 m $\text{s}^{-1}$ | 02-017 | $2.32 \times 10^4$ | 1.01 | −3.34 | −0.584 |
| | | 02-027 | $2.36 \times 10^4$ | 1.07 | −2.98 | −0.490 |
| | | 02-028 | $2.53 \times 10^4$ | 1.06 | −2.27 | −0.361 |
| 0.5 | 1.5 m $\text{s}^{-1}$ | 05-004 | $9.04 \times 10^3$ | 1.37 | −1.45 | −0.298 |
| | | 05-010 | $9.12 \times 10^3$ | 1.27 | −1.38 | −0.316 |
| | 7.0 m $\text{s}^{-1}$ | 05-007 | $3.06 \times 10^4$ | 1.57 | −7.52 | −1.310 |
| | | 05-009 | $2.81 \times 10^4$ | 1.59 | −7.54 | −1.320 |

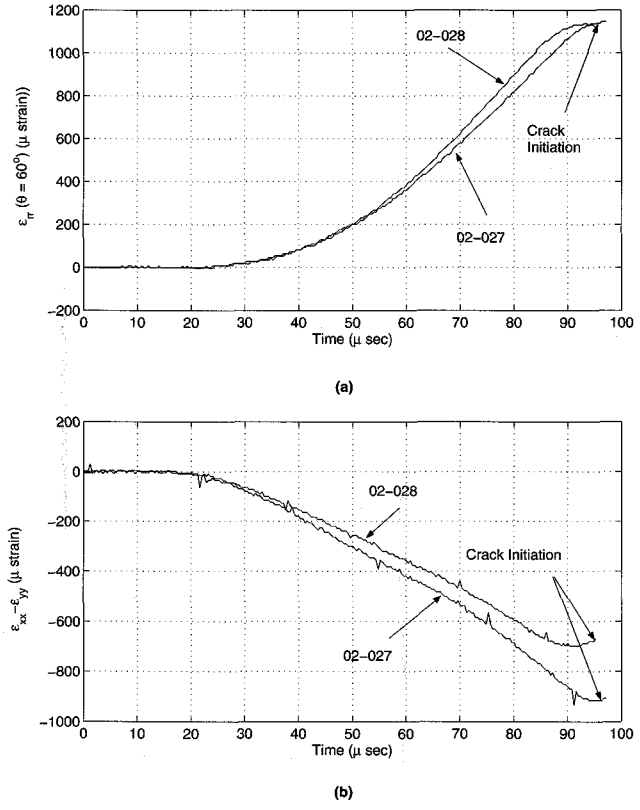


Fig. 12. Typical strain histories for (a) $K_I$ and (b) $T$-gages for two different specimens (02-027 and 02-028) with $a/W = 0.2$ and $V = 7.0$ m $\text{s}^{-1}$

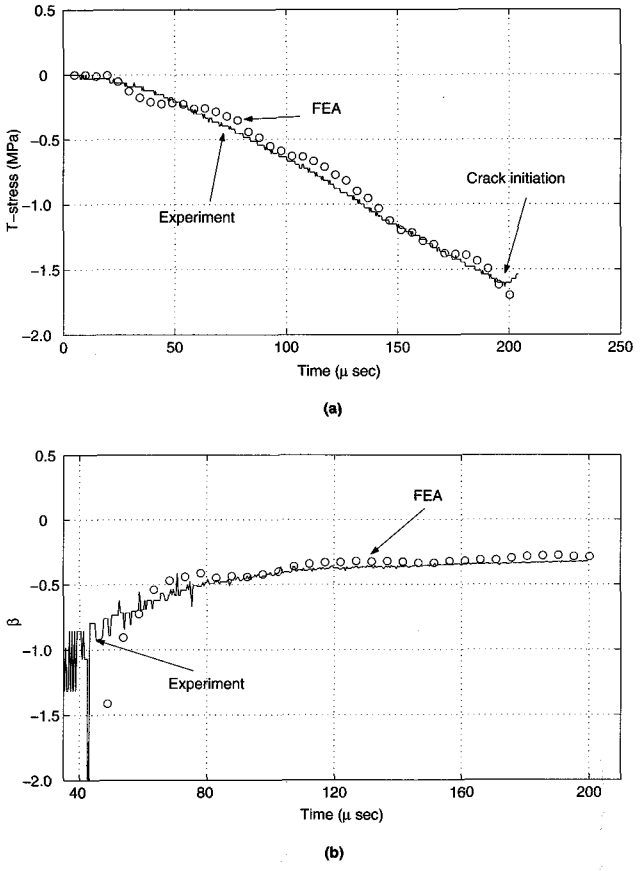


Fig. 13. Comparison of experimental and finite element analysis results for $a/W$ = 0.2 and an impact velocity of 1.5 m $\text{s}^{-1}$. Variation of (a) $T$-stress with time and (b) $\beta$ with time

which is between $6.0 \times 10^3$ and $6.3 \times 10^3$ MPa $\sqrt{\text{m}}$ $\text{s}^{-1}$ for an impact velocity of 1.5 m $\text{s}^{-1}$. Similarly, for an impact velocity of 7.0 m $\text{s}^{-1}$, the crack tip loading rate is in the range $2.8 \times 10^4$ to $3.0 \times 10^4$ for deeply cracked specimens, whereas for shallow cracked specimens these values are $2.3 \times 10^4$ to $2.5 \times 10^4$. Secondly, the increase in $\beta$ is more pronounced for deeply cracked specimens than for shallow cracked specimens as impact velocity increases. The cumulative effect from the above two phenomena can manifest itself to cause a significant enhancement in the fracture toughness under dynamic loading conditions. Similar trends have been reported by Jayadevan et al.[6] in their numerical simulations. However, additional experiments with higher impact velocities are needed to confirm the observed trends. The crushing of epoxy at the impact point imposes an upper limit for tup velocity. Also, larger specimens are to be employed to preclude impact point interactions at higher values of $a/W$ ratios.

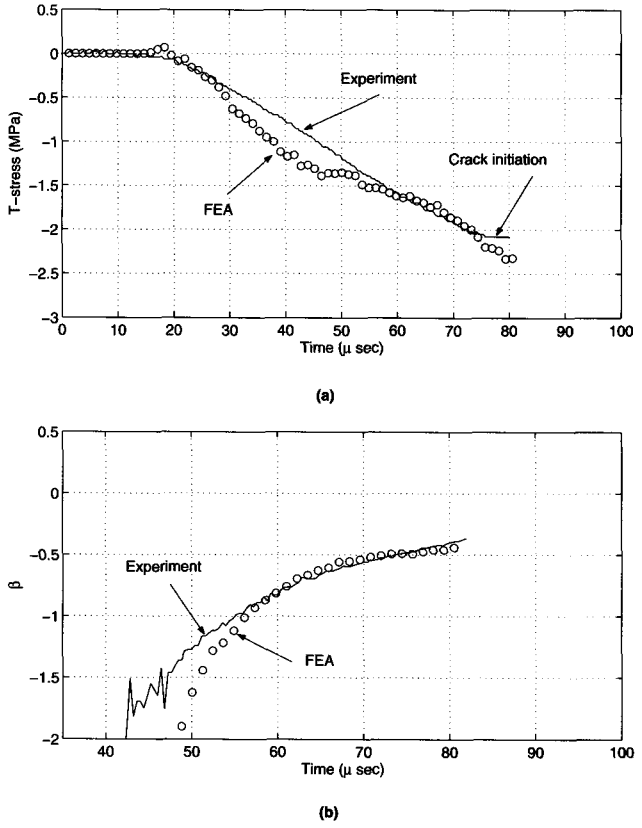


Fig. 14. Comparison of experimental and finite element analysis results for $a/W$ = 0.2 and an impact velocity of 7.0 m $s^{-1}$. Variation of (a) $T$-stress with time and (b) β with time

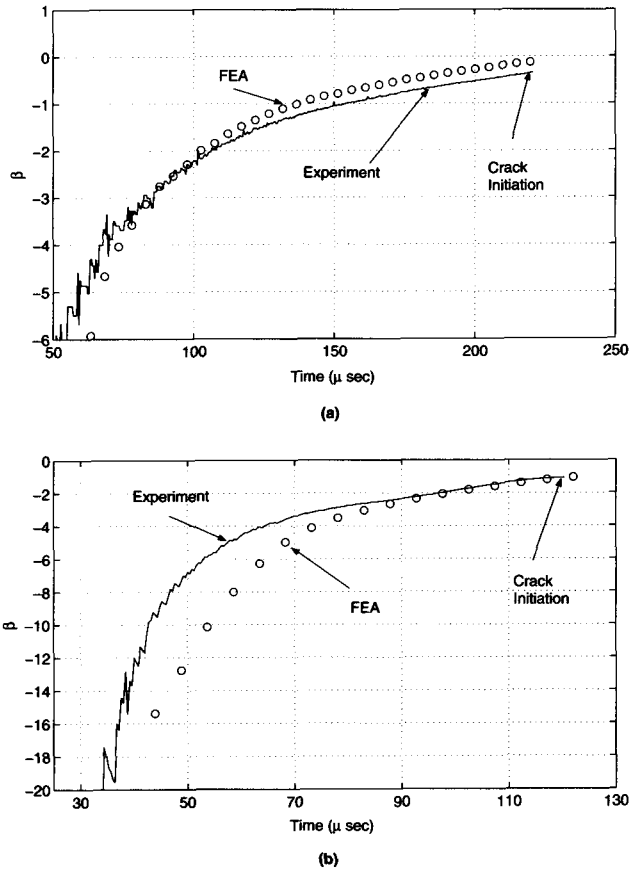


Fig. 15. Comparison of experimental and finite element analysis results for $a/W$ = 0.5. Variation of β with time for an impact velocity of (a) 1.5 m $s^{-1}$ and (b) 7.0 m $s^{-1}$

## Conclusions

We have proposed an experimental method of determining $T$-stress near a mode I crack using a stacked strain gage rosette. The measurements have been performed under static as well as low-velocity impact loading conditions on edge-cracked epoxy beams in symmetric TPB and one-point impact configurations. The crack tip SIF histories have been measured using the Dally–Sanford method in order to obtain the crack tip biaxiality parameter β history up to crack initiation. Combining $T$-stress and $K_I$ values, β histories are also extracted. The experimental measurements are examined along with independent finite element computations.

The following conclusions are drawn from the present study.

1. Among the different options considered, $r = 0.55B$, $\theta = 120°$ ($r$ and θ are polar coordinates centered around the crack tip and $B$ is the specimen thickness) was found to be optimum for locating a stacked 0°–90° gage rosette to measure $T$-stress using two-term approximation.

2. The experimentally determined time histories of β are in close agreement with those predicted from finite element simulations for shallow cracked specimens.

3. The crack tip loading rate is higher for deeply cracked specimens compared to shallow cracked specimens for the same impact velocity.

4. Crack initiation toughness increases with impact velocity. This effect is more pronounced for deeply cracked specimens. This is accompanied by a more negative β at higher impact velocities in deeply cracked specimens.

5. Additional experiments are needed to study constraint effects over a wide range of impact velocities and crack length to specimen width ratios.

### Acknowledgments

The authors gratefully acknowledge the support of the research through grants ARMY-DAAD19-01-1-0745 (equipment) and NSF-CMS-9912066. The authors would also like to thank Professor R.J. Sanford, University of Maryland-College Park, and Professor R. Narasimhan, Indian Institute of Science, for their suggestions during this research.

### References

*1. Richardson, D.E. and Goree, J.G., "Experimental Verification of a New Two-parameter Fracture Model," ASTM-STP, Vol. 1189, American Society for Testing and Materials, Philadelphia, PA, 738–750 (1993).*

*2. Chao, Y.J., Liu, S., and Broviak, B.J., "Brittle Fracture: Variation of Fracture Toughness with Constraint and Crack Curving Under Mode I Conditions," EXPERIMENTAL MECHANICS, **41** (3), 232–241 (2001).*

*3. Irwin, G.R., "Discussion of the Dynamic Stress Distribution Surrounding a Running Crack – A Photoelastic Analysis," Proceedings of the Society of Experimental Stress Analysis, **16** (1), 93–96 (1957).*

*4. Kirk, M.T., Koppenhoefer, K.C., and Shih, C.F., "Effect of Constraint on Specimen Dimensions Needed to Obtain Structurally Relevant Toughness*

*Measures," Constraint Effects in Fracture, ASTM-STP, Vol. 1171, American Society for Testing and Materials, Philadelphia, PA, 79–103 (1993).*

*5. Koppenhoefer, K.C. and Dodds, R.H., "Constraint Effects on Fracture Toughness of Impact-loaded, Pre-cracked Charpy Specimens," Journal of Nuclear Engineering and Design,* **162** *(2–3), 145–158 (1996).*

*6. Jayadevan, K., Narasimhan, R., Ramamurthy, T., and Dattaguru, B., "A Numerical Study in Dynamically Loaded Fracture Specimens," International Journal of Solids and Structures,* **38**, *4987–5005 (2001).*

*7. Sanford, R.J., Principles of Fracture Mechanics, Prentice-Hall, Englewood Cliffs, NJ (2002).*

*8. Chona, R., Irwin, G.R., and Sanford, R.J., "Influence of Specimen Size and Shape on the Singularity-dominated Zone," Fracture Mechanics 14th Symposium, Vol. 1: Theory and Analysis, ASTM-STP, Vol. 791, American Society for Testing and Materials, Philadelphia, PA, 492–502 (1983).*

*9. Tippur, H.V., Krishnaswamy, S., and Rosakis, A.J., "Optical Mapping of Crack Tip Deformations Using the Methods of Transmission and Reflection Coherent Gradient Sensing: A Study of Crack Tip K-dominance," International Journal of Fracture,* **52**, *91–117 (1991).*

*10. Ramulu, M. and Kobayashi, A.S., "Mechanics of Crack Curving and Branching—A Dynamic Fracture Analysis," EXPERIMENTAL MECHANICS,* **27**, *187–201 (1985).*

*11. Sumter, J.D.G., "An Experimental Investigation of the T-stress Approach: Constraint Effects in Fracture," ASTM-STP, Vol. 1171, American Society for Testing and Materials, Philadelphia, PA, 492–502 (1993).*

*12. Larsson, S.G. and Carlsson, A.J., "Influence of Non-singular Stress Terms on Small Scale Yielding at Crack Tips in Elastic–plastic Materials," Journal of the Mechanics and Physics of Solids,* **21**, *263–277 (1973).*

*13. Rice, J.R., "Limitations to the Small-scale Yielding Approximations for Crack Tip Plasticity," Journal of the Mechanics and Physics of Solids,* **22**, *17–26 (1974).*

*14. Kfouri, A.P., "Some Evaluations of the Elastic T-term using Eshelby's Method," International Journal of Fracture,* **30**, *301–315 (1986).*

*15. Nakamura, T. and Parks, D.M., "Determination of Elastic T-stress along Three-dimensional Crack Fronts Using Interaction Integral," International Journal of Solids and Structures,* **29**, *1597–1611 (1992).*

*16. Sladek, J., Sladek, V., and Fedelinski, P., "Integral Formulation for Elastodynamic T-stresses," International Journal of Fracture,* **84**, *103–116 (1997).*

*17. Yang, B. and Ravi-Chandar, K., "Evaluation of Elastic T-stress by Stress Difference Method," Engineering Fracture Mechanics,* **64**, *589–601 (1999).*

*18. Dally, J.W. and Sanford, R.J., "Strain Gage Methods for Measuring the Opening-mode Stress Intensity Factor, $K_I$," EXPERIMENTAL MECHANICS,* **49**, *381–388 (1987).*

*19. Dally, J.W. and Sanford, R.J., "Measuring the Stress Intensity Factor for Propagating Cracks with Strain Gages," Journal of Testing and Evaluation,* **18** *(4), 240–249 (1990).*

*20. Westergaard, H.M., "Bearing Pressure and Cracks," ASME Journal of Applied Mechanics,* **6** *(1939).*

*21. Williams, M.L., "On the Stress Distribution at the Base of a Stationary Crack," Journal of the Mechanics and Physics of Solids,* **24**, *109–114 (1957).*

*22. Rosakis, A.J. and Ravi-Chandar, K., "On Crack-tip Stress State: An Experimental Evaluation of Three-dimensional Effects," International Journal of Solids and Structures,* **22**, *121–138 (1986).*

*23. Rousseau, C.E. and Tippur, H.V., "Dynamic Failure of Compositionally Graded Materials with Cracks Along the Elastic Gradient: Experiments and Analysis," Mechanics of Materials,* **33**, *403–421 (2001).*

*24. Anderson, T.L., Fracture Mechanics: Fundamentals and Applications, 2nd edition, CRC Press, New York (1994).*

*25. O'Dowd, N.P. and Shih, C.F., "Two Parameter Fracture Mechanics: Theory and Applications," ASTM-STP, Vol. 1207, American Society for Testing and Materials, Philadelphia, PA, 21–47 (1994).*